Research Square

Preprints are preliminary reports that have not undergone peer review.
They should not be considered conclusive, used to inform clinical practice,
or referenced by the media as validated information.

Light-Driven Controlled Liquid Manipulation by 3D-Printed Elastomers

Giovanni Simonetti
University of Florence
Ruggero Rossi
University of Florence
Daniele Martella
University of Florence
Diederik Sybolt Wiersma
diederik.wiersma@unifi.it
University of Florence
Camilla Parmeggiani
University of Florence

Article

Keywords: Liquid crystalline elastomers, 4D printing, photothermal response, smart materials, contactless fluidics

Posted Date: November 26th, 2026

DOI: https://doi.org/10.21203/rs.3.rs-11800230/v1

License: This work is licensed under a Creative Commons Attribution 4.0 International License.
Read Full License

Additional Declarations: No competing interests reported.

Light-Driven Controlled Liquid Manipulation by 3D-Printed Elastomers

Giovanni Simonetti, Ruggero Rossi, Daniele Martella, Diederik Sybolt Wiersma* and Camilla Parmeggiani*

G. Simonetti, D.S. Wiersma
Department of Physics and Astronomy, University of Florence, via Sansone 1, 50019, Sesto Fiorentino, Italy

R. Rossi, D. Martella, C. Parmeggiani
Department of Chemistry "Ugo Schiff", University of Florence, via della Lastruccia 13, 50019, Sesto Fiorentino, Italy

G. Simonetti, D. Martella, D.S. Wiersma, C. Parmeggiani
European Laboratory for Non Linear Spectroscopy (LENS), via N. Carrara 1, Sesto Fiorentino, 50019, Italy

E-mail: ruggero.rossi@unifi.it, diederik.wiersma@unifi.it

Keywords: *Liquid crystalline elastomers, 4D printing, photothermal response, smart materials, contactless fluidics.*

Abstract

Liquid crystal elastomers (LCEs) represent key materials for soft actuators, combining polymer elasticity with liquid crystalline order to enable large and programmable deformations. Doping LCEs with photoresponsive dyes allows for fast, contactless light activation suitable for delicate environment operations. 3D printing by Direct Ink Writing (DIW) provides precise spatial control over mesogen alignment, but a systematic investigation on the combined role of the chemical composition and the dye on the final material behavior is still missing. Here, we present a comprehensive study correlating the mesogen ratio and dye functionalization directly to the thermomechanical and actuation properties of DIW-printed LCEs. To isolate these effects, we separately characterize dye undoped and doped LCE formulations, systematically evaluating how molecular composition and dye addition influence the final mechanical performance and thermal response. Interestingly, while both classes of materials exhibit strong

reversible thermal contraction, the dye-doped LCEs demonstrate rapid photoactuation, achieving fast mechanical responses on hundreds of millisecond timescales under short light pulses. Guided by these systematic results, we select the top-performing formulation to fabricate a light-driven soft pump as a proof-of-concept device. This 3D-printed actuator enables reproducible, contactless aspiration and ejection of fluids through localized light stimulation, offering a versatile platform for remotely controlled bioinspired devices and microfluidic systems.

Introduction

Liquid Crystalline Elastomers (LCEs) are materials containing aligned mesogenic units and combining the optical anisotropy and self-organization of liquid crystals with the structural stability of crosslinked polymers.[1,2] This mentioned structural stability is accompanied by the typical viscoelastic mechanical behavior of elastomers, given by a low crosslinking density and a glass transition temperature below room temperature.[3] The result is the obtainment of polymers capable of a reversible and controlled shape deformation in response to an external stimulus such as heat,[4,5] light,[6,7] or electromagnetic fields.[8–10] Conventional fabrication methods, such as cell infiltration followed by photocuring, have extensively established how the mesogen structure, quantity, and stoichiometry dictate the final crosslinked network properties. Therefore, the quantity of mesogenic monomers can be adjusted to tune the liquid crystal phase transition temperature and, consequently, the temperature range over which actuation occurs.[11]

4D printing, the 3D printing of responsive materials, has recently emerged as a powerful additive manufacturing technique for LCEs fabrication,[12] as it widens the range of their possible actuation patterns and dimensions (from nm to cm), and minimizes the operator dependency in the materials fabrication. As many different techniques are used, the 4D printing of LCEs is used already for applications in soft robotics,[13,14] biomedics,[15,16] adaptive optics[17–19] and microfluidics.[20] Direct Ink Writing (DIW), in particular, allows the simultaneous fabrication and programming of LCEs structures by controlling the molecular alignment during the printing process. Indeed, the shear stress generated within the nozzle during extrusion, as shown in **Figure 1a,** aligns the mesogens along the printing direction. Consequently, the deposition path establishes the axis of the molecular director, which ultimately determines the contraction direction when the LCE is exposed to a trigger, as displayed in **Figure 1b**. This intrinsic coupling between the printing path and the molecular alignment allows the fabrication of

complex, customized, and multifunctional structures with programmable and spatially controlled actuation including bending,[21] twisting,[22] rolling,[23] expansion[24] and contraction.[25]

To obtain a smooth and uniform extrusion during DIW of LCEs, the ink formulation needs to be properly designed to provide suitable flow and simultaneous alignment, while preserving the liquid crystalline properties of the material.[26] LC inks are commonly prepared through thiol–ene or thiol–amine Michael addition between the acrylate groups of reactive mesogens and dithiols or diamines, respectively, to obtain an extrudable oligomer containing the LC moieties into its backbone.[3,27] Under a covalent crosslinking strategy, the curing process is usually initiated during the extrusion and completed after. A suitable photoinitiator is used, providing a mechanically stable elastomeric matrix while preserving the programmed molecular alignment. When the ink is formulated with a stoichiometric excess of acrylate groups, the crosslinking proceeds via the unreacted acrylate moieties remaining from oligomerization. Conversely, an initial excess of dithiols needs the addition of a crosslinking agent, such as a vinylic one.[28] Furthermore, the addition of photoresponsive moieties into LC inks imparts light responsiveness, enabling remote, localized, and highly controllable actuation without physical contact. Azobenzene dyes are widely employed as photoswitchable molecules[29] capable of undergoing reversible *trans-cis* isomerization upon UV/visible light exposure, consequently, macroscopic actuation without the need for direct heating. In general, the force generated by LCEs under light irradiation can arise from two distinct mechanisms: a photochemical contribution, originating from the *trans–cis* photoisomerization of the azobenzene moieties and the resulting disruption of the liquid crystalline order, and a photothermal contribution, resulting from the conversion of absorbed light into heat, also leading to the partial disruption of the liquid crystal order.[30] Azobenzene diacrylates[31–33] are commonly directly incorporated into the oligomeric backbone, providing a strong and durable photoactuation. On the other hand, the use of a monoacrylate push-pull azobenzene as Disperse Red 1 Acrylate (DR1A) provides a much cost effective functionalization and provides reportedly fast photoactuations, generating a significant tension within 100 ms of irradiation.[18] As DR1A is monofunctional, its direct addition to the oligomerization mixture acts as a chain terminator, greatly reducing the oligomer length and altering the final properties of both the ink and the printed material. Although the effects of oligomer composition, and azobenzene functionalization on LCE properties have been studied independently,[34–36] their combined investigation within a unified, DIW-printable ink has received little attention.

Starting from our previous demonstration about 3d printing optimization for LCEs frabrication[18], we now systematically investigated the synthetic approach, by finely tuning the

ink formulation, demonstrating the importance of mesogen ratio and dye incorporation, and their combined effects, on the LC printable inks properties. While systematically characterizing the influence of the mesogens ratios within the mixture formulation, the LC inks have been used to obtain both dye-doped and non-doped DIW-printed LCEs, that have been studied in their thermomechanical behavior and actuation performances. Varying the oligomer composition allows us to tune the mesophase stability, chain mobility and mechanical response of the resulting elastomer, providing a rational framework for selecting the formulation best suited to DIW printability and shape-programming.

Building on this formulation study, we elucidated how the presence of the azobenzene dye affects the ink properties and the LCEs actuation performances, thanks to a comparative characterization investigating the impact of DR1A on the thermal, mechanical, and molecular alignment behavior of the LCE matrix. Overall, the obtained results established a versatile framework for engineering DIW-printable LC inks with tailored thermomechanical and photoactuation properties.

The best performing formulation in terms of tension generated under light irradiation has been used to fabricate a functional, light-actuated soft robotic device. Indeed, a proof-of-concept demonstration of a light-driven soft pump was studied, as represented in **Figure 1c**. This device serves as an illustrative example of a contactless soft system capable of controlled, light driven liquid aspiration and ejection of a liquid from a pipette. This demonstrator highlights the potential of the 3D printed photoresponsive LCEs in optical control for fluidic applications where the transport of milliliters of liquids is necessary.

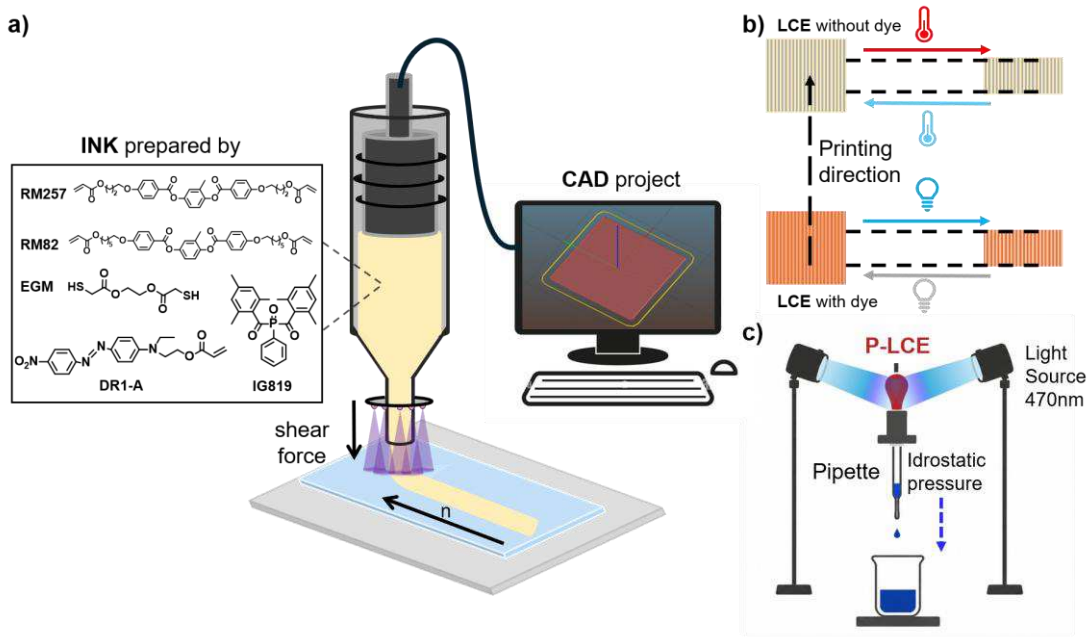

Figure 1. Direct ink writing of liquid crystalline elastomers and set-up for light-driven contactless liquid manipulation. (a) Schematic representation of the DIW additive manufacturing process and molecular structures of the ink components; (b) Illustration of the LCE actuation mechanism in response to thermal and light stimuli; (c) Representation of the light-driven, contactless LCE soft pump.

Results

Development and Characterization of LC-Based Inks

LC-based inks for DIW were prepared via a Michael thiol–acrylate addition reaction, a well-established strategy for the synthesis of LCE precursors.[37] In this approach, diacrylate mesogens were reacted with an aliphatic dithiol to generate liquid crystalline oligomers. A thiol to acrylate molar ratio of 1:1.2 was employed, leaving a controlled excess of acrylate groups available for subsequent covalent photopolymerization after printing, thereby ensuring a sufficient crosslinking density in the printed elastomer. Furthermore, three LC ink formulations were prepared by varying the relative proportions of the commercial diacrylate mesogens RM82 and RM257 while maintaining a constant total mesogen moles content. The selected RM82:RM257 molar ratios were 1:2, 1:1 and 2:1, hereafter referred to as Mix1, Mix2, and Mix3, respectively reported in **Table 1**. The corresponding crosslinked elastomers are denoted as LCE1, LCE2, and LCE3 throughout the manuscript. Each formulation contained the dithiol chain extender ethylene glycol bis(mercaptoacetate) (EGM), 2 wt% of the photoinitiator Irgacure 819, and 1 wt% triethylamine (TEA) as the catalyst. For the photoresponsive formulations, 1 wt% of the azobenzene derivative Disperse Red 1 Acrylate (DR1A) was additionally incorporated directly in the reaction mixtures described above (all chemical structures are reported in Figure 1a).

These formulations are referred to as P-Mix1, P-Mix2, and P-Mix3, with the prefix P denoting the photoresponsive formulations relative to their non-doped counterparts. All the Michael thiol–acrylate addition reactions were carried out in dichloromethane (DCM) at 50 °C under magnetic stirring for 2h.

Table 1. Composition of LC inks used for DIW process. The total diacrylates to dithiol molar ratio (m.r.) is fixed as 1.2:1. The weight percentage (wt%) of DR1A is calculated on the sum of the diacrylates and dithiol masses.

Mixture ID	RM82/RM257 m.r.	EGM m.r.	DR1A [wt%]	T_{NI} [°C]
Mix 1	1/2	1	-	68
Mix 2	1/1	1	-	72
Mix 3	2/1	1	-	77
P-Mix 1	1/2	1	1	68
P-Mix 2	1/1	1	1	70
P-Mix 3	2/1	1	1	77

The TEA catalyst was then removed by liquid–liquid extraction using an acidic aqueous solution. A detailed description of the synthesis and purification procedures is provided in the Supporting Information with the corresponding ^{1}H-NMR spectra in Figure S1.

By combining Polarized Optical Microscopy (POM) images with Differential Scanning Calorimetry (DSC) thermograms (Figure S2a), the liquid crystalline phase and the corresponding phase transition temperatures were identified for each formulation. The three mixtures exhibited a single endothermic peak, corresponding to the nematic-to-isotropic transition (T_{NI}), occurring at 68 °C, 72 °C, and 77 °C for Mix1, Mix2, and Mix3, respectively. The DSC analysis revealed that increasing the RM82 content shifted the T_{NI} toward higher temperatures. The higher molecular weight of RM82 increases the overall mesogen mass fraction relative to the isotropic dithiol chain extender, which raises T_{NI} consistently with previously reported dependencies on the mesogen molecular weight,[35] where increasing the spacer length also led to stiffer LCE networks. The same was observed for the photoresponsive counterparts containing the azobenzene dye (Figure S2b). Specifically, the incorporation of 1 wt% DR1A did not produce any significant change in the nematic-to-isotropic transition temperature for any of the three formulations, indicating that the photoresponsive dopant does not alter the liquid crystalline phase behavior at the investigated concentration.

4D Printing and LCE characterization

All LCE specimens were fabricated using a Hyrel 3D Engine Standard Resolution (ESR) printer equipped with a 25G nozzle (inner diameter 0.254 mm) and a screw-driven extrusion system operating at 1800 rpm. A series of rectangular strips with dimensions of 10 x 3 x 0.1 mm^3 were printed using the same printing parameters for all the inks. Printing was performed at an extrusion temperature of 100 °C and a printing speed of 5 mm/s. The extrusion temperature was selected to maintain the LC ink in the isotropic phase within the syringe, thereby ensuring a homogeneous flow. Upon extrusion, the temperature gradient between the heated syringe and the nozzle tip induced cooling of the material into the liquid crystalline phase, while the shear stresses generated inside the nozzle promoted mesogen alignment along the printing direction.

The molecular alignment of the printed LCEs, both with and without DR1A, was evaluated by POM. The optical anisotropy of the well-aligned LCEs produces a periodic modulation in the light transmission as the sample rotates between crossed polarizers, showing alternating transmission maxima and minima at 45° intervals. Representative POM images of 100 μm-thick LCE2 samples and their photoresponsive counterparts are shown in **Figure 2a**, confirming that mesogen alignment is oriented along the printing direction. Corresponding POM images for LCE1, LCE3, and the DR1A-containing formulations are provided in the Supporting Information Figure S3a-c.

Following printing, all specimens were exposed to UV light (Thorlabs M385LP1, λ = 385 nm) for 20 min to complete the photocuring of the residual acrylate groups, yielding fully crosslinked elastomeric networks.

The printing and photopolymerization of Mixes 1–3 and their DR1-A–doped counterparts yielded the corresponding LCEs: LCE1–3 and P-LCE1–3.

DSC measurements of the LCEs were performed over the temperature range from −30 °C to 180 °C. As shown in Figure S4**,** the thermograms exhibited no detectable thermal transitions, consistent with the formation of a fully crosslinked elastomeric network. No evidence of degradation or residual phase transitions was observed, as expected for chemically crosslinked LCEs.

The thermomechanical behavior of the printed LCEs was characterized by Dynamic Mechanical Analysis (DMA). The temperature dependence of the storage modulus (E') and the dumping factor (tan δ) was evaluated for all the formulations (**Figures 2b-c**), providing insight into the influence of mesogen composition and azobenzene incorporation on the mechanical response of the crosslinked networks.

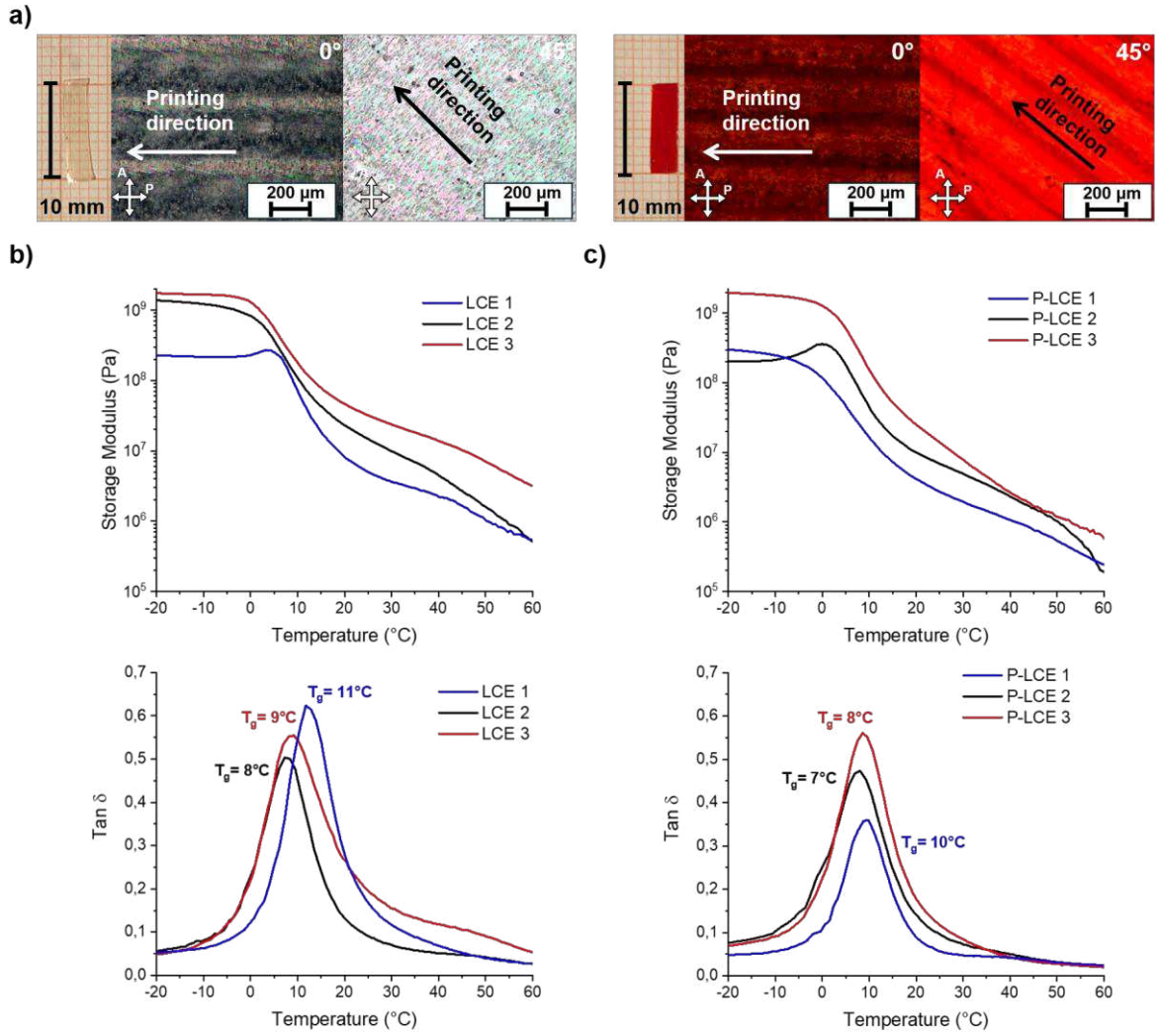

Figure 2. Molecular alignment and thermomechanical characterization of undoped (LCE) and dye-doped (P-LCE) 3D-printed elastomers. (a) POM images of LCE2 and the corresponding DR1A-containing formulation at 0° and 45° with respect to the polarizer axis. The variation in optical transmittance between the two orientations confirms the alignment of the LCE mesogens along the printing direction; (b) DMA characterization of the three LCE formulations performed in tensile mode at a heating rate of 5 °C/min. The storage modulus (E′) and tan(δ) are shown as a function of temperature, with the tan(δ) peak corresponding to the glass transition temperature T_g; (c) DMA characterization of the DR1A-containing LCE formulations under the same experimental conditions.

The DMA results, summarized in **Table 2**, are consistent with the DSC analysis of the LC mixtures, confirming that increasing the RM82 content enhances the stiffness of the crosslinked network. Specifically, the storage modulus (E') measured at 25 °C increased from 5 MPa for LCE1 to 14 MPa for LCE2, reaching 30 MPa for LCE3. This trend is consistent with the different spacer length of the reactive mesogen. Moreover, RM82 contains a longer spacer length than RM257, and increasing its content increases the average spacer length within the polymer network. The longer spacer promotes greater mesogen mobility during network formation, leading to a higher storage modulus.

An opposite trend was observed for the Tan δ curves. Increasing the RM257 content resulted in a slight increase in the glass transition temperature T_g, which was determined from the peak of the tan δ curve. LCE1 exhibited the highest T_g (10 °C), whereas LCE2 and LCE3 showed T_g values of 8 °C and 9 °C, respectively. The small differences observed among the three formulations suggest that the mesogen composition does not significantly affect the glass transition temperature.

A different trend was observed for the LCEs containing the azobenzene dye. While the glass transition temperature T_g remained essentially unchanged for all three formulations, the storage moduli are significantly lower than the ones from the undoped LCEs. Indeed, the storage modulus at 25 °C decreased to 14 MPa for the RM82-rich formulation (P-LCE3), while values of 7 MPa and 3 MPa were measured for P-LCE2 and P-LCE1, respectively. Interestingly, the composition dependent trend remained the same of the undoped LCEs, as also in this case the increasing in the RM82 quantity leads to an increase in the storage modulus. These results indicate that DR1A acts as a mild plasticizer within the elastomeric network. Notably, as it increases the network flexibility and lowers the storage modulus, it does not alter the glass transition or broader thermal behavior at this investigated concentration.

Thermal actuation comparison

LCEs typically undergo structural deformation when heated above a specific threshold. This shape change arises from reduced orientational order among the mesogens, which causes the material to contract along the director (*n*) and expand perpendicularly. To assess thermal response, rectangular samples (10 x 3 x 0.1 mm^3) were heated on a hot plate and photographed at 10 °C intervals. **Figure 3** shows the temperature dependence of the normalized sample length (L/L_0), defined relative to room temperature.

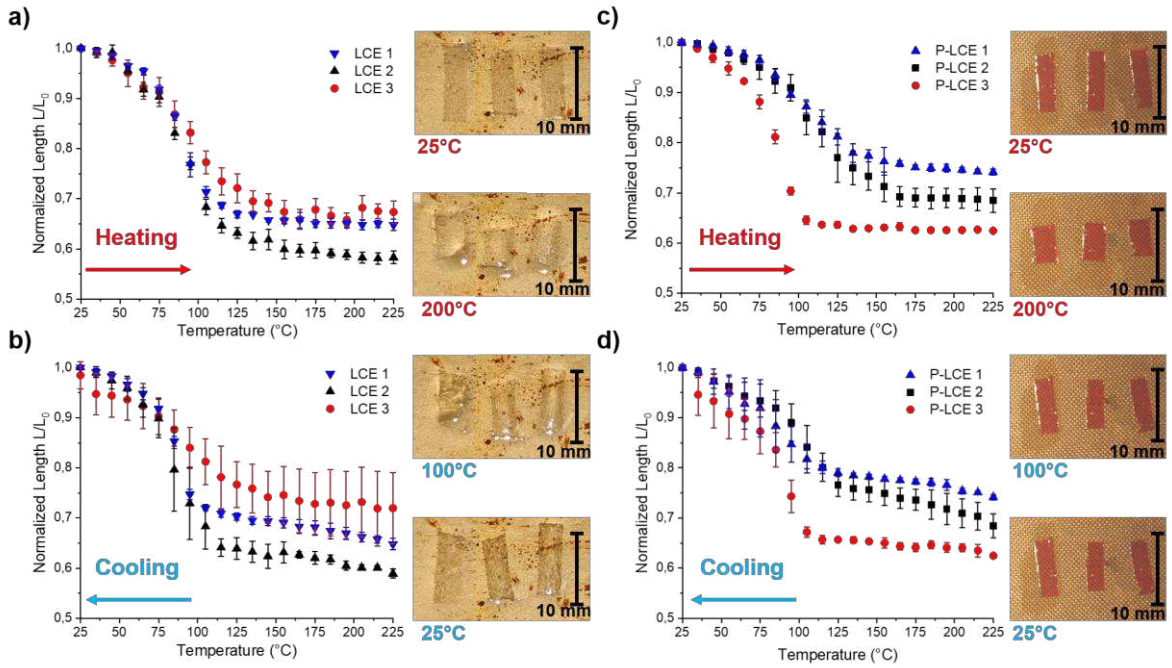

Figure 3. Reversible thermal actuation of printed undoped (LCE) and dye-doped (P-LCE) elastomers. (a) Thermal contraction and (b) recovery behavior of rectangular LCE samples during heating and cooling at a rate of 10 °C/min, together with representative images acquired during the thermal actuation cycle; (c-d) Thermal actuation and recovery of the DR1A-containing LCE formulations under the same heating and cooling conditions.

The thermally induced actuation behavior of the printed LCEs was evaluated by monitoring the contraction strain as a function of temperature. As the temperature increased, all the LCEs exhibited a gradual increase in contraction, reaching a plateau at approximately 150 °C. As shown in **Figure 3a**, the maximum contraction strains of the undoped LCEs were 36%, 42%, and 33% for LCE1, LCE2, and LCE3, respectively.

Upon cooling to room temperature, all samples fully recovered their original shape, **Figure 3b**, demonstrating the reversible and elastic nature of the thermally induced actuation.

The incorporation of the azobenzene dye affected the thermomechanical response, leading to a reduction in the maximum contraction strain for two of the three formulations. As shown in **Figure 3c**, the maximum strain decreased by approximately 10% for P-LCE1 and P-LCE2, whereas P-LCE3 exhibited virtually unchanged actuation performance. This behavior is consistent with the DMA results, which revealed a reduction in the storage modulus of the dye doped formulations while preserving their thermal transition temperatures. **Figure 3d** demonstrates the completely elastic return, as mentioned in Figure 3b, for dye formulation as well.

Table 2. Summary of the LC ink properties and the thermomechanical and actuation performance of the corresponding LCEs.

LCE # ID	T_g [°C]	E'(25°C) [MPa]	ε max [%]	σ (8s) max [kPa]	σ (250ms) max [kPa]
LCE 1	11	5	36	X[a)]	X[a)]
LCE 2	8	14	42	X[a)]	X[a)]
LCE 3	9	30	33	X[a)]	X[a)]
P-LCE 1	10	3	25	172±61	11±4
P-LCE 2	7	7	32	211±31	14±1
P-LCE 3	8	13	36	236±21	18±1

[a)]Formulation without photoresponsive azobenzene.

Photoactuation in isometric condition

The photomechanical performance of the printed LCEs was characterized using a custom-built setup previously developed to measure isometric tension under light irradiation.[38–40] LCE strips (20 x 1.2 x 0.1 mm³) were vertically mounted between a force transducer and a fixed support, as illustrated in **Figure 4a**. The samples were irradiated simultaneously from both sides by two 470 nm LEDs, with a fixed optical power density at 15.9 mW/mm^2 to investigate its influence on the generated force.

An initial series of experiments was performed on 100 µm-thick LCE strips to evaluate the relationship between the generated tension and the incident optical power density. The samples were subjected to repeated illumination cycles consisting of 8 s of light exposure followed by 2 s in the dark (**Figure 4b**). During each irradiation period, the generated tension increased rapidly before reaching a plateau after approximately 5 s. Once the illumination was removed, the stress returned to its initial value within approximately 2 s, demonstrating the reversible photoactuation of the three LCEs. As demonstrated in previous works, the photoactuation of the DR1A-doped LCEs is governed by a combination of photothermal and photochemical mechanisms, whereby light absorption by the azobenzene chromophore generates heat that triggers the thermally driven contraction of the LCE network.[18] Consequently, the enhanced photoactuation performance of P-LCE3 reflects its intrinsically superior thermoactuation capability, promoted by the RM82-rich anisotropic network. Under these conditions, P-LCE3 generated the highest maximum stress, reaching approximately 240 kPa. For comparison, P-LCE1 and P-LCE2 reached maximum stresses of 173 kPa and 211 kPa, respectively. To evaluate the repeatability of the photoactuation, the LCE strips were subjected to four

consecutive irradiation cycles using the same 8 s ON/2 s OFF protocol. Representative results from the first four cycles are shown in Figure S5, demonstrating a highly reproducible response with negligible cycle-to-cycle variation.

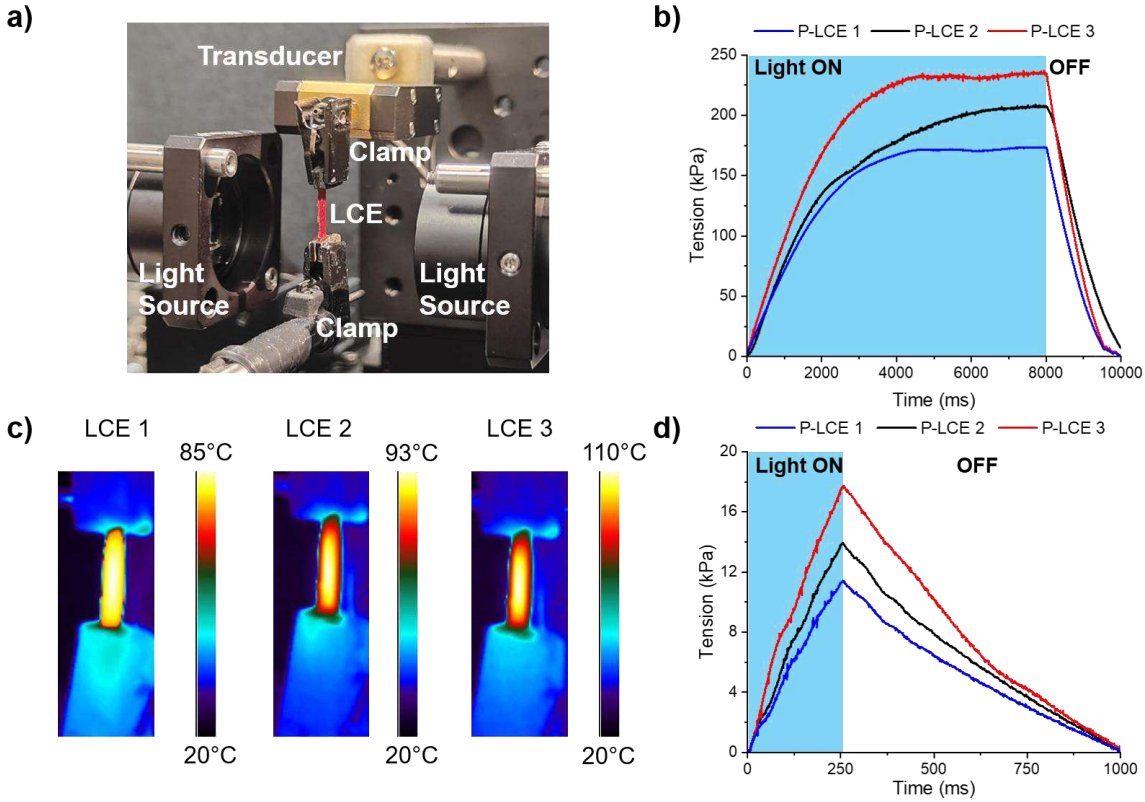

Figure 4. Set-up configuration and light-induced force generation of dye-doped LCEs. (a) Schematic illustration of the experimental setup used for isometric photoactuation measurements, (b) Photoactuation response of the DR1A-containing LCE formulations under 8 s irradiation cycles; (c) Thermal images of 100 µm-thick samples of the three LCE formulations during 8 s of continuous irradiation. (d) Photoactuation response of 100 µm-thick LCE samples under short 250 ms light pulses.

To identify the dominant mechanism between the photochemical and photothermal actuation under our experimental conditions, the surface temperature of the LCEs strips was monitored during isometric photoactuation.

Representative thermal images of a 100 µm-thick LCE during an 8 s irradiation period are shown in **Figure 4c**. Upon illumination, all formulations exhibited a significant temperature increase, indicating efficient photothermal conversion. Among them, P-LCE3 reached the highest temperature, increasing by approximately 90 °C to a maximum of about 110 °C. In comparison, P-LCE1 and P-LCE2 reached maximum temperatures of approximately 85 °C and 93 °C, respectively. The higher equilibrium temperature attained by P-LCE3 correlates with its superior photoactuation performance, suggesting that both mechanisms play a key role

simultaneously in the driving force generation under the investigated irradiation conditions. Although a photochemical contribution from azobenzene isomerization cannot be excluded, the strong correlation between the equilibrium temperature and the generated stress indicates that photothermal heating to be the predominant actuation mechanism under these experimental conditions.

A second series of photoactuation experiments was performed under short-pulse irradiation to evaluate the dynamic response of the printed LCEs to stimuli on the order of hundreds of milliseconds. Such operating conditions are particularly relevant for applications requiring rapid and sensitive actuation, including biomedical devices,[38] artificial muscles[36,41] and soft sensors.[42]

As shown in **Figure 4d**, the three P-LCE formulations were subjected to cyclic stimulation consisting of 250 ms irradiation time at an optical power density of 15.9 mW/mm², followed by a 750 ms relaxation period. Consistent with the long-pulse experiments, P-LCE3 exhibited the highest actuation performance, generating a maximum stress of approximately 18 kPa. However, the performance gap between the three formulations was less pronounced under these conditions, with P-LCE1 and P-LCE2 producing maximum stresses of approximately 11 kPa and 14 kPa, respectively.

The repeatability of the fast photoactuation was further evaluated through twenty activation–relaxation cycles (Figures S6), which demonstrated a stable and reproducible mechanical response over repeated stimulations. These results confirm the ability of the printed LCEs to respond within a few hundred milliseconds while maintaining consistent actuation, underscoring their suitability for applications requiring rapid, cyclic, and dynamic operation. All the data referred to the maximum tension developed are reported in Table 2.

LCE soft pump driven by light

The applicability of our approach to soft robotic and fluidic devices was preliminarily demonstrated through the fabrication of a DIW-printed, light-actuated soft pump. The device was designed to exploit the actuation properties of the LCEs to modulate the internal pressure of the bulb, enabling the controlled aspiration and release of liquids with good robustness and reproducibility.

Based on its superior photoactuation performance P-LC3 was selected as the active material for this proof-of-concept pumping device. Moreover, qualitative evaluation of the liquid release triggered by P-LCE actuation was performed. We measured the time required to release a drop of solution under an optical stimulus of 436 mW/mm². The device architecture consists of two

rectangular LCE strips (40 × 10 × 0.1 mm³) attached around the upper portion of a commercial latex bulb. A standard pipette tip compatible with P1000 micropipettes was inserted into the lower part of the bulb to enable liquid handling. A water solution containing 5 µg/ml methylene blue (MB) was prepared to help the visualization of the liquid during the experiment.

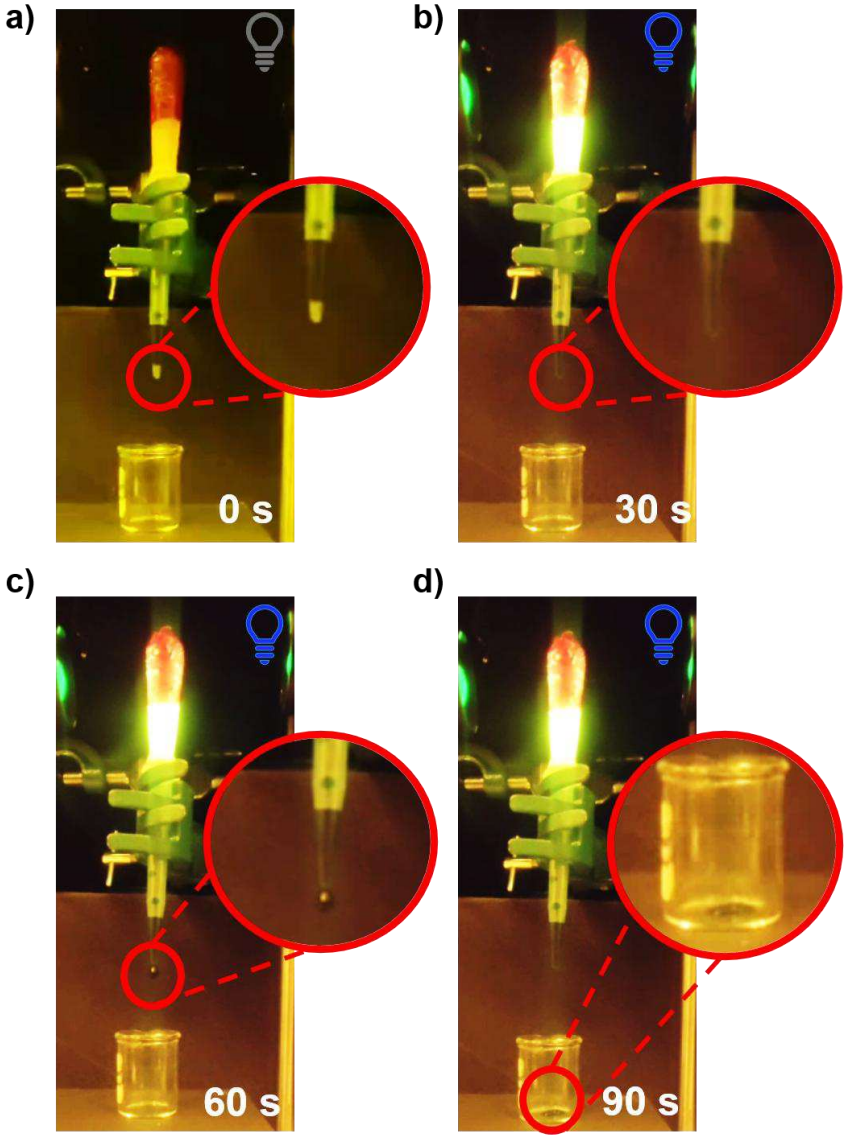

Figure 5. Light-driven contactless ejection of a liquid by the LCE soft actuator. (a) Initial state (0 s), with the pipette loaded with MB solution and no fluid motion. (b) After 30 s of irradiation, photoactuation of the P-LCE generates a positive pressure inside the latex bulb, initiating liquid downward movement within the pipette. (c) After 60 s, the first droplet emerges from the pipette tip. (d) Complete droplet release is achieved after 90 s of continuous irradiation. Magnified insets highlight the evolution of the droplet during the dispensing process.

In the initial state, the pipette is loaded with 200 µl of solution, as shown in **Figure 5a**, and the system remains under static conditions with no detectable fluid motion. When the light stimulus is applied to the LCE device, it generates a positive pressure inside the bulb, initiating a

downward movement of the liquid solution within the pipette, as displayed in **Figure 5b**. After 60 s of continuous optical stimulation, the first drop emerged from the pipette tip **Figure 5c**. Complete drop release was achieved after 90 s from the onset of irradiation, as illustrated in (**Figure 5d**). A sped-up video of multiple drop releases is reported in SI Movie S1.

A further step was to evaluate the complete pumping cycle, including both liquid aspiration and ejection. A schematic illustration of the experimental setup of the light-driven LCE pumping device is presented in **Figure 6a**. Aqueous methylene blue (MB) solutions (5 μg/ml) with different densities were used to investigate the pumping performance under identical operating conditions. Importantly, the P-LCE actuators do not come into direct contact with the transported liquid, even though they reach relatively high temperatures during photoactuation. This contactless operating mechanism makes the device particularly attractive for microfluidic applications involving thermally sensitive, biological, or chemically reactive fluids, where preventing direct exposure to the heat source is essential.

In the initial configuration, the empty pipette tip was immersed in the solution and it operates through alternating 1.5 min illumination from two symmetric light sources (470 nm, 436 mW/mm^2) and 1.5 min of dark relaxation phases. During the light-ON phase, the photoactuation of the P- LCE3 strips compresses the latex bulb, expelling trapped air in the initial cycle and the liquid in the following cycles. By switching the light off, the elastic recovery of the LCEs restores the bulb to its original shape, generating a negative pressure that aspirates the solution into the pipette tip, as shown in **Figure 6b** and Movie S2.

The repeatability of the pumping system was evaluated over three consecutive actuation cycles. Furthermore, to assess the versatility of the device, the pumping performance was investigated using three model liquids with different densities. Specifically, three model fluids with different densities were investigated: distilled water, phosphate buffered saline solution (PBS 1x), and a saturated aqueous NaCl solution, with measured densities of 0.97, 0.99, and 1.14 g/ml, respectively. As expected, the aspiration height depended on the density of the working fluid, as shown in **Figure 6c**. According to the hydrostatic pressure relationship described by Stevin's law (**Equation 1**), where ΔP represents the hydrostatic pressure or the change in pressure between two points, ρ the density of the fluid, g is the gravitational acceleration and h is the height of the fluid column above the point of measurement, a higher liquid density requires a higher pressure difference to achieve the same aspiration height. Figure S7 reports the pressure gradient developed by the LCEs during the aspiration phase; depending on the liquid aspired, the exerted pressure is calculated between 55 and 60 Pa.

Equation 1 $\Delta P = \rho g h$

Therefore, for a given pressure generated by the LCE actuator, less dense fluids can be aspirated to greater heights. Accordingly, the average aspiration height was 6.33 mm for distilled water, decreasing to 5.60 mm for PBS and 4.81 mm for the saturated NaCl solution, which exhibited the highest density. These results demonstrate the ability of the light-actuated LCE soft pump to reproducibly transport liquids with different physicochemical properties, while highlighting the influence of fluid density on the pumping performance.

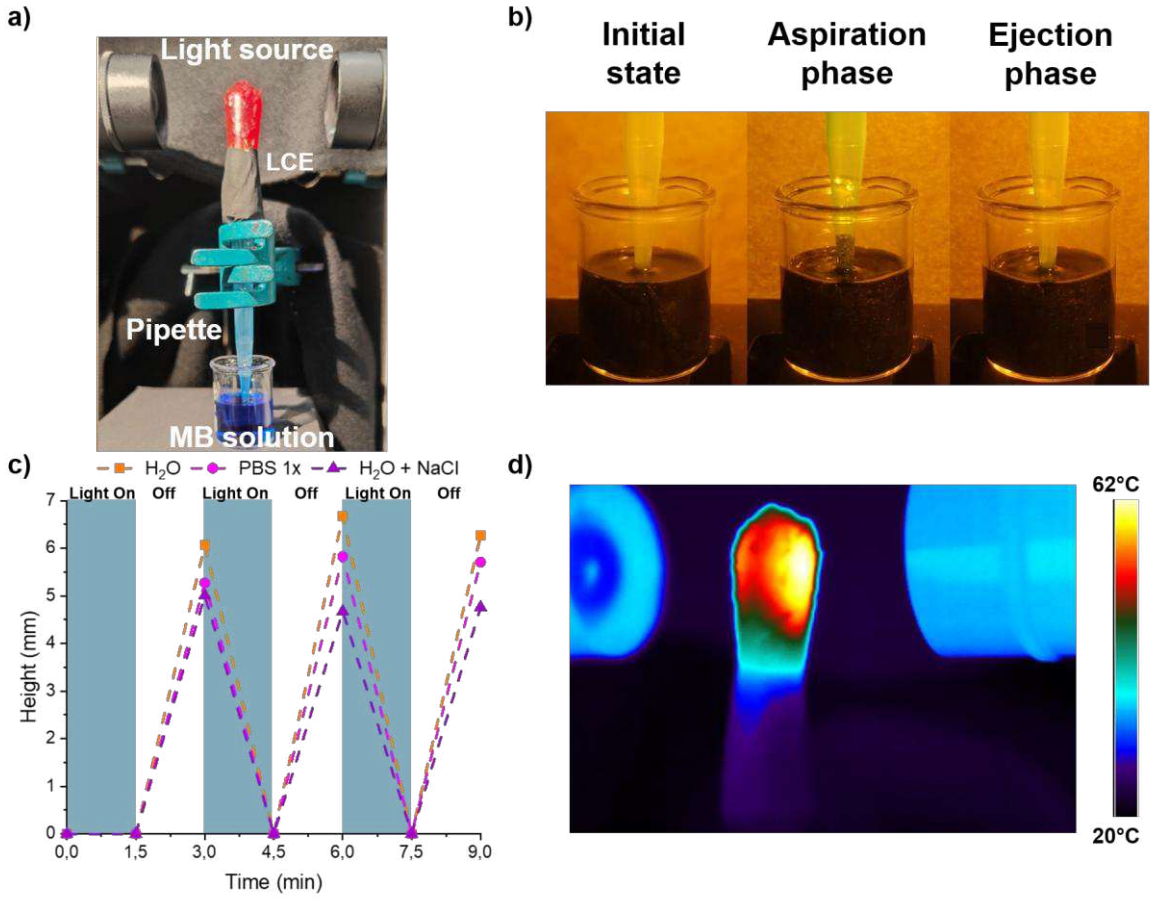

Figure 6. Light-driven contactless aspiration and ejection of liquids using an LCE soft actuator. (a) Illustration of the light-driven LCE soft pump device and experimental setup. (b) Representative images of the pipette tip during liquid ejection and aspiration over a complete light-actuation cycle. (c) Aspiration height of the liquid measured over multiple actuation cycles of the LCE soft pump using fluids with different densities. (d) Thermal image of the LCE soft pump device during light irradiation.

Finally, the surface temperature of the device was monitored by infrared thermal imaging during light irradiation (**Figure 6d**). Under the operating conditions employed for the pumping experiments, the LCE strips reached a maximum temperature of approximately 62 °C during the aspiration phase. Since this temperature is considerably lower than that achieved during the

isometric photoactuation experiments, where photothermal actuation was found to dominate, these results suggest that photothermal heating alone cannot fully explain the pumping behavior. Instead, they indicate that the photochemical contribution arising from azobenzene photoisomerization is likely to become increasingly relevant under these milder irradiation conditions. Moreover, as the heating is localized on the irradiated parts, it prevents the evaporation or the thermal degradation of the aspirated and dispensed fluids. By consequence, this system is suitable for the handling of delicate or thermally sensitive liquids within sensitive environments.

Discussions

Through the design of inks for the 3D printing of LCEs, and their counterparts doped with the azobenzene dye DR1A, we studied the relationship between the monomers' ratio and the thermomechanical and actuation properties of the printed materials. This initial study demonstrated how adjusting the ratio between the mesogens leads to materials with distinct mechanical properties, while highlighting the non-trivial relationship between mechanical performance and actuation behavior. DR1A doping exerted a plasticizing effect that significantly lowered the elastic moduli of the printed materials by 42% to 47%, reducing maximum contraction by roughly 10%, with the notable exception of the RM82-rich P-LCE3, which retained its full thermal performance. Interestingly, comparing the doped and undoped materials revealed no significant changes in transition temperatures (both Tg and T_{NI}), indicating that the presence of the dye did not disrupt the order of the nematic phase.

In terms of photoactuation, the printed LCEs generated significant and repeatable isometric stresses on the order of hundreds of kilopascals under blue-light irradiation, reaching a maximum of approximately 240 kPa for P-LCE3 after less than 10 s of illumination. Under short-pulse irradiation (250 ms), the materials were also capable of producing stresses up to 18 kPa, demonstrating a rapid and reproducible response on the timescale required for dynamic actuation. These results highlight the potential of the proposed DIW-printable LCE platform for applications requiring fast, remotely controlled, and contactless actuation, such as optical systems, soft robotics, and sensing technologies. To showcase its functional utility, we transformed a rubber pipette bulb into a light-driven soft actuator capable to manipulate a fluid by integrating 3D-printed strips of our P-LCE3 material onto the bulb. When the LCEs are illuminated with blue light (436 mW/mm^2), they contract and squeeze the bulb, expelling air or fluid, at a rate of one drop each 90 seconds of irradiation. When the light is removed, the LCEs relax and the bulb draws liquid (or air) inside the pipette. The LCE soft pump aspirated and

ejected liquid reproducibly, and the height of the aspirated liquid depended on the solution density, with denser liquids reaching lower heights for the same light-driven suction. By correlating the height reached by each fluid during the aspiration phase to Stevin's law, the pressure variation was calculated to be between 55 and 60 Pa. To the best of our knowledge, this is the first example of a fully wireless system for controlling fluid suction and ejection at the milliliter scale. Together, these results establish our DIW-printable LCE platform as a versatile route to remotely controlled, contactless actuation, with clear promise for optical systems, soft robotics, sensing, and microfluidic devices.

Experimental Methods

Materials

Reactive mesogens 1,4-bis-[4-(6-acryloyloxyhexyloxy)benzoyloxy]-2-methylbenzene (RM82) and 1,4-bis[4-(3-acryloyloxypropyloxy) benzoyloxy]-2-methylbenzene (RM257) were purchased from Angene Chemical. The dithiol chain extender ethyleneglycolbis-mercaptoacetate (EGM) and UV photoinitiator phenyl bis(2,4,6-trimethyl benzoyl), also referred to as Irgacure 819 (IG819) were purchased from Merck, as well as the base catalyst Triethylamine (TEA) and dichloromethane (DCM). The azobenzene dye Disperse Red 1 Acrylate (DR1A) was obtained from Specific Polymers. All reagents were used as received.

Printing Equipment. Samples were fabricated using a Hyrel Engine Standard Resolution 3D printer (Hyrel 3D, Norcross, GA, USA), which provides an XY positioning accuracy of ±50 µm and a Z-axis accuracy of ±10 µm. The printer was equipped with a Tambora (TAM) high-temperature extrusion head and an integrated UV-LED array. Printing was performed directly onto microscope cover glass substrates (24 × 50 × 0.1 mm^3). During the printing process, the deposited layer was photopolymerized in situ using the integrated 365 nm UV-LED array. After printing, the samples were subjected to a post-curing step under a 385 nm UV light source (M385LP1-C4, Thorlabs) with an irradiance of 0.22 mW/mm^2 for 20 min at room temperature.

Characterization methods

The NMR spectra were recorded with a Varian Gemini 200 MHz instrument.

The morphology and alignment of the printed structures were examined by light microscopy using an inverted microscope (Zeiss Axio Observer A1) operated with or without crossed polarizers.

Thermal transitions were investigated by Differential Scanning Calorimetry (DSC) using a Q2000 calorimeter (TA Instruments, Milan, Italy) under a nitrogen atmosphere. Heating and cooling scans were performed at a rate of 20 °C/min.

The thermomechanical properties of the printed polymer were characterized by Dynamic Mechanical Analysis (DMA 8000, PerkinElmer) in tensile mode. Rectangular specimens (20 × 3 × 0.1 mm³) were heated from −20 °C to 60 °C at a rate of 5 °C/min. The glass transition temperature (T_g) was determined from the first peak of the tan(δ) curve, while the storage modulus (E') at 25 °C evaluated the elastic components of LCE.

Thermal actuation

Thermally induced contraction was evaluated on uniaxially aligned printed LCE strips (10 × 3 × 0.1 mm³) immersed in silicone oil and placed on a Mettler Toledo HS82 programmable hot plate. Samples were heated from 25 °C to 225 °C at a rate of 10 °C/min. Images were acquired every 10 °C using Hasselblad camera system on One Plus 11, and the resulting dimensional changes were quantified with ImageJ software.

Photoactuation

The photoinduced stress generated by the LCEs was measured using a custom-built setup previously described. The system consisted of a force transducer (WPI KG4, 0–50 mN) in which the LCE strip was mounted between two clamps under isometric conditions. Samples were simultaneously irradiated from both sides using two M470L5 LEDs (Thorlabs), while light exposure was controlled through a LabVIEW interface connected to a multichannel driver. Photoactuation experiments were performed under pulsed irradiation with optical power densities at 15.9 mW/mm². The developed stress (σ) was calculated according to Equation 2:

$$\textbf{Equation 2}\ \sigma = F/A_{cs}$$

where F is the measured force (mN) and A_{cs} is the irradiated sample cross-sectional area (mm²).

Thermal imaging

The surface temperature of the LCE samples during photoirradiation was monitored using a FLIR A500 thermal imaging camera. Measurements were performed under the same experimental conditions adopted for the 8-second photoactuation test.

For the pumping set up a commercial latex bulb was covered at the higher tip by two LCEs strips (dimension 40 x 10 x 0.1 mm³), while in the lower part was inserted a standard pipette tip compatible with P1000 micropipettes. The device was clamped to a holder and covered with

black tape to avoid speckle reflection by the bulb during the recording. The pipette tip is soaked in three different solutions (distilled water, phosphate buffered saline solution 1x and saturated aqueous NaCl solution) coloured by 5 μg/ml methylene blue concentration.

Author Contribution Statement

G.S. synthesized the LC inks, performed the thermomechanical, thermal and photoactuation characterization, analysed the data and wrote the original draft of the manuscript. R.R. conceived and supervised the study, contributed to design the ink formulations, performed NMR spectra and edited the manuscript. D.M. contributed to conceptualization and methodology and reviewed the manuscript. D.S.W. supervised the project and reviewed the manuscript. C.P. conceived and supervised the study, acquired funding, and reviewed and edited the manuscript. All authors discussed the results and approved the final version of the manuscript.

Acknowledgements

This work has received funding from MUR under the program "Dipartimenti di Eccellenza 2023-2027" within the project won by the Department of Chemistry “Ugo Schiff” (DICUS 2.0).

Competing interests

All authors declare no financial competing interests.

Data Availability

The data that supports the findings of this study are available in the supplementary material of this article.

Supporting Information

Supporting Information is available from the NPJ soft matter or from the author.

References

1. White, T. J. & Broer, D. J. Programmable and adaptive mechanics with liquid crystal polymer networks and elastomers. *Nat. Mater.* **14**, 1087–1098 (2015).
2. Terentjev, E. M. Liquid Crystal Elastomers: 30 Years After. *Macromolecules* **58**, 2792–2806 (2025).

3. Del Pozo, M., Sol, J. A. H. P., Schenning, A. P. H. J. & Debije, M. G. 4D Printing of Liquid Crystals: What's Right for Me? *Adv. Mater. Deerfield Beach Fla* **34**, e2104390 (2022).
4. McDougall, L. *et al.* Free-Form Liquid Crystal Elastomers via Embedded 4D Printing. *ACS Appl. Mater. Interfaces* **15**, 58897–58904 (2023).
5. Maurin, V. *et al.* Liquid Crystal Elastomer–Liquid Metal Composite: Ultrafast, Untethered, and Programmable Actuation by Induction Heating. *Adv. Mater.* **36**, 2302765 (2024).
6. Das, G., Jo, H. & Park, S.-Y. Low-temperature reprogrammable dual light-responsive liquid crystalline elastomer films. *Chem. Eng. J.* **466**, 143368 (2023).
7. Skillin, N. P. *et al.* Photothermal Actuation of Thick 3D-Printed Liquid Crystalline Elastomer Nanocomposites. *Adv. Mater.* **36**, 2313745 (2024).
8. Ohm, C., Brehmer, M. & Zentel, R. Liquid Crystalline Elastomers as Actuators and Sensors. *Adv. Mater.* **22**, 3366–3387 (2010).
9. Feng, C. *et al.* Electroresponsive Ionic Liquid Crystal Elastomers. *Macromol. Rapid Commun.* **40**, 1900299 (2019).
10. Davidson, Z. S. *et al.* Monolithic shape-programmable dielectric liquid crystal elastomer actuators. *Sci. Adv.* **5**, eaay0855 (2019).
11. Donato, S. *et al.* What is the right chain length? Liquid Crystalline Network tuning by molecular design. *Macromolecules*.
12. Wan, X., Luo, L., Liu, Y. & Leng, J. Direct Ink Writing Based 4D Printing of Materials and Their Applications. *Adv. Sci.* **7**, 2001000 (2020).
13. López-Valdeolivas, M., Liu, D., Broer, D. J. & Sánchez-Somolinos, C. 4D Printed Actuators with Soft-Robotic Functions. *Macromol. Rapid Commun.* **39**, (2018).

14. Yang, Q. *et al.* Four-waveband-modulated liquid crystal elastomer (LCE) actuators for soft robotics based on optical wavelength selective actuation of dye-doped LCE materials. *Chem. Eng. J.* **529**, 172892 (2026).
15. Roach, D. J. *et al.* Long Liquid Crystal Elastomer Fibers with Large Reversible Actuation Strains for Smart Textiles and Artificial Muscles. *ACS Appl. Mater. Interfaces* **11**, 19514–19521 (2019).
16. Li, S. *et al.* Spider-Inspired Helically Engineered Fiber-Based Artificial Muscle with Coupled Actuation and Self-sensing Capabilities. *Adv. Fiber Mater.* **8**, 1653–1665 (2026).
17. Nocentini, S., Martella, D., Wiersma, D. S. & Parmeggiani, C. Beam steering by liquid crystal elastomer fibres. *Soft Matter* **13**, 8590–8596 (2017).
18. Simonetti, G. *et al.* 4D printing of fast-responsive liquid crystalline elastomers for light-driven actuators. *Responsive Mater.* **4**, e70039 (2026).
19. Morimoto, R., Ogata, M., Matsumoto, K., Shimonomura, K. & Tsutsumi, O. Multilayer Mechanical Transduction Activates Compression-Mode Mechano-Optical Response in Chiral Nematic Liquid Crystal Elastomers. *Aggregate* **7**, e70438 (2026).
20. Fleischmann, E.-K., Forst, F. R. & Zentel, R. Liquid-Crystalline Elastomer Fibers Prepared in a Microfluidic Device. *Macromol. Chem. Phys.* **215**, 1004–1011 (2014).
21. Lu, X. *et al.* 4D-Printing of Photoswitchable Actuators. *Angew. Chem. Int. Ed.* **60**, 5536–5543 (2021).
22. Escobar, M. C. & White, T. J. Fast and Slow-Twitch Actuation via Twisted Liquid Crystal Elastomer Fibers. *Adv. Mater.* **36**, 2401140 (2024).
23. Ahn, C., Li, K. & Cai, S. Light or Thermally Powered Autonomous Rolling of an Elastomer Rod. *ACS Appl. Mater. Interfaces* **10**, 25689–25696 (2018).
24. Velasco Abadia, A., Bauman, G. E., White, T. J., Schwartz, D. K. & Kaar, J. L. Direct Ink Writing of Enzyme-Containing Liquid Crystal Elastomers as Versatile Biomolecular-Responsive Actuators. *Adv. Mater. Interfaces* **10**, 2300086 (2023).

25. Chen, W., Wang, R. & Liu, K. Active compliant mechanisms for optimized actuation by LCE-based artificial muscles. *Mech. Mater.* **189**, 104879 (2024).
26. Głowińska, E., Parcheta, P. & Datta, J. Chapter 10 - Rheology of liquid crystalline polymers. in *Rheology of Polymer Blends and Nanocomposites* (eds Thomas, S., Sarathchandran, C. & Chandran, N.) 205–224 (Elsevier, 2020). doi:10.1016/B978-0-12-816957-5.00010-0.
27. Carothers, K., Gibson, J., Carrola, M., Selhorst, R. & Auguste, A. The influence of ink preparation on the properties of 3D-printed liquid crystal elastomers. *Soft Matter* **22**, 5546–5555 (2026).
28. Bauman, G. E., McCracken, J. M. & White, T. J. Actuation of Liquid Crystalline Elastomers at or Below Ambient Temperature. *Angew. Chem. Int. Ed Engl.* **61**, e202202577 (2022).
29. Pilz Da Cunha, M., Van Thoor, E. A. J., Debije, M. G., Broer, D. J. & Schenning, A. P. H. J. Unravelling the photothermal and photomechanical contributions to actuation of azobenzene-doped liquid crystal polymers in air and water. *J. Mater. Chem. C* **7**, 13502–13509 (2019).
30. Lee, K. M. & White, T. J. Photochemical Mechanism and Photothermal Considerations in the Mechanical Response of Monodomain, Azobenzene-Functionalized Liquid Crystal Polymer Networks. *Macromolecules* **45**, 7163–7170 (2012).
31. Lugger, S. J. D., Ceamanos, L., Mulder, D. J., Sánchez-Somolinos, C. & Schenning, A. P. H. J. 4D Printing of Supramolecular Liquid Crystal Elastomer Actuators Fueled by Light. *Adv. Mater. Technol.* **8**, 2201472 (2023).
32. Ceamanos, L. *et al.* Four-Dimensional Printed Liquid Crystalline Elastomer Actuators with Fast Photoinduced Mechanical Response toward Light-Driven Robotic Functions. *ACS Appl. Mater. Interfaces* **12**, 44195–44204 (2020).

33. Sartori, P., Singh Yadav, R., Barrio, J. del, DeSimone, A. & Sánchez-Somolinos, C. Photochemically induced propulsion of a 4D printed liquid crystal elastomer biomimetic swimmer. https://doi.org/10.13039/501100000781 (2024) doi:10.13039/501100000781.
34. White, T. J. Photomechanical Effects in Liquid-Crystalline Polymer Networks and Elastomers. in *Photomechanical Materials, Composites, and Systems* 153–177 (John Wiley & Sons, Ltd, 2017). doi:10.1002/9781119123279.ch5.
35. Saed, M. O. *et al.* Molecularly-Engineered, 4D-Printed Liquid Crystal Elastomer Actuators. *Adv. Funct. Mater.* **29**, 1806412 (2019).
36. Donato, S. *et al.* The Role of Crosslinker Molecular Structure on Mechanical and Light-Actuation Properties in Liquid Crystalline Networks. *Macromol. Rapid Commun.* **44**, 2200958 (2023).
37. Li, Y. *et al.* Liquid Crystalline Elastomers Based on Click Chemistry. *ACS Appl. Mater. Interfaces* **14**, 14842–14858 (2022).
38. Ferrantini, C. *et al.* Development of Light-Responsive Liquid Crystalline Elastomers to Assist Cardiac Contraction. *Circ. Res.* **124**, e44–e54 (2019).
39. Turriani, M. *et al.* Exploiting photopolymerization to modulate liquid crystalline network actuation. *Soft Matter* **21**, 1162–1169 (2025).
40. Feregotto, G. *et al.* Direct Ink Printing of Liquid Crystalline Elastomers Towards Photoresponsive Artificial Muscles. in *3D Printing and Bioprinting in Medicine and Surgery* (eds Carfagni, M., Celi, S., Servi, M. & Mencarelli, M.) 33–44 (Springer Nature Switzerland, Cham, 2025). doi:10.1007/978-3-031-94626-4_5.
41. Vitale, G. *et al.* Photoresponsive Polymer-Based Biomimetic Contractile Units as Building Block for Artificial Muscles. *Macromol. Mater. Eng.* **307**, 2200187 (2022).
42. Spinoso, V., Concas, R., Martella, D. & Nocentini, S. Temperature Capacitive Sensors Based on Liquid Crystalline Gels. *ACS Appl. Mater. Interfaces* https://doi.org/10.1021/acsami.6c12680 (2026) doi:10.1021/acsami.6c12680.

Supporting Information

Light-Driven Controlled Liquid Manipulation by 3D-Printed Elastomers

Giovanni Simonetti, Ruggero Rossi, Daniele Martella, Diederik Sybolt Wiersma* and Camilla Parmeggiani*

Synthesis of the mixtures

Synthesis of Mix 1:

768 mg of RM82 (1.14 mmol, 0.4 eq.), 1344 mg of RM257 (2.28 mmol, 0.8 eq.) and 54 mg of IG819 (0.12 mmol, 0.05 eq.) were dissolved in 10 mL of DCM, then 600 mg of EGM (2.8 mmol, 1.0 eq.) and 27 mg of TEA (0.26 mmol, 0.09 eq.) were added. The mixture was stirred continuously at 50 °C for 2 h, then washed with water. The organic layers were dried over sodium sulphate and the solvent removed under reduced pressure. The product was obtained with quantitative yield as a white solid.

Synthesis of Mix 2:

1152 mg of RM82 (1.72 mmol, 0.6 eq.), 1008 mg of RM257 (1.72 mmol, 0.6 eq.) and 56 mg of IG819 (0.14 mmol, 0.05 eq.) were dissolved in 10 mL of DCM, then 600 mg of EGM (2.8 mmol, 1.0 eq.) and 27.6 mg of TEA (0.28 mmol, 0.10 eq.) were added. The mixture was stirred continuously at 50 °C for 2 h, then washed with water. The organic layers were dried over sodium sulphate and the solvent removed under reduced pressure. The product was obtained with quantitative yield as a white solid.

Synthesis of Mix 3:

1536 mg of RM82 (2.28 mmol, 0.8 eq.), 672 mg of RM257 (1.14 mmol, 0.4 eq.) and 56 mg of IG819 (0.12 mmol, 0.05 eq.) were dissolved in 10 mL of DCM, then 600 mg of EGM (2.8 mmol, 1.0 eq.) and 28 mg of TEA (0.28 mmol, 0.10 eq.) were added. The mixture was stirred continuously at 50 °C for 2 h, then washed with water. The organic layers were dried over sodium sulphate and the solvent removed under reduced pressure. The product was obtained with quantitative yield as a white solid.

Synthesis of P-Mix 1:

768 mg of RM82 (1.14 mmol, 0.4 eq.), 1344 mg of RM257 (2.28 mmol, 0.8 eq.), 27 mg of DR1A (0.08 mmol, 0.03 eq.) and 54 mg of IG819 (0.12 mmol, 0.05 eq.) were dissolved in 10 mL of DCM, then 600 mg of EGM (2.8 mmol, 1.0 eq.) and 27 mg of TEA (0.26 mmol, 0.09 eq.) were added. The mixture was stirred continuously at 50 °C for 2 h, then washed with water. The organic layers were dried over sodium sulphate and the solvent removed under reduced pressure. The product was obtained with quantitative yield as a red solid.

Synthesis of P-Mix 2:

1152 mg of RM82 (1.72 mmol, 0.6 eq.), 1008 mg of RM257 (1.72 mmol, 0.6 eq.), 27.6 mg of DR1A (0.08 mmol, 0.03 eq.) and 56 mg of IG819 (0.14 mmol, 0.05 eq.) were dissolved in 10 mL of DCM, then 600 mg of EGM (2.8 mmol, 1.0 eq.) and 27.6 mg of TEA (0.28 mmol, 0.10 eq.) were added. The mixture was stirred continuously at 50 °C for 2 h, then washed with water. The organic layers were dried over sodium sulphate and the solvent removed under reduced pressure. The product was obtained with quantitative yield as a red solid.

Synthesis of P-Mix 3:

1536 mg of RM82 (2.28 mmol, 0.8 eq.), 672 mg of RM257 (1.14 mmol, 0.4 eq.), 28 mg of DR1A (0.08 mmol, 0.03 eq.) and 56 mg of IG819 (0.12 mmol, 0.05 eq.) were dissolved in 10 mL of DCM, then 600 mg of EGM (2.8 mmol, 1.0 eq.) and 28 mg of TEA (0.28 mmol, 0.10 eq.) were added. The mixture was stirred continuously at 50 °C for 2 h, then washed with water.

The organic layers were dried over sodium sulphate and the solvent removed under reduced pressure. The product was obtained with quantitative yield as a red solid.

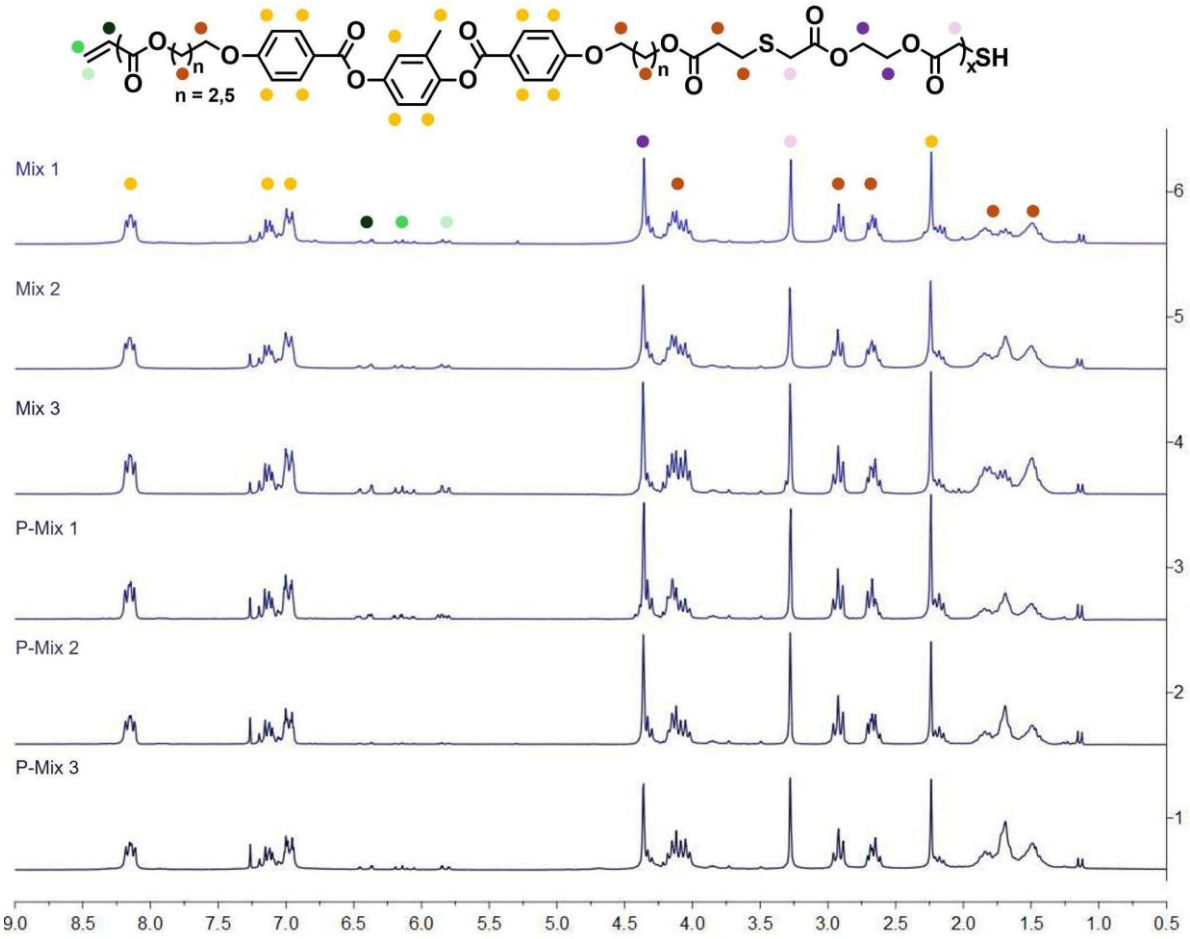

Figure S1: ^{1}H-NMR spectra (200MHz, $CDCl_3$) of the proposed mixtures.

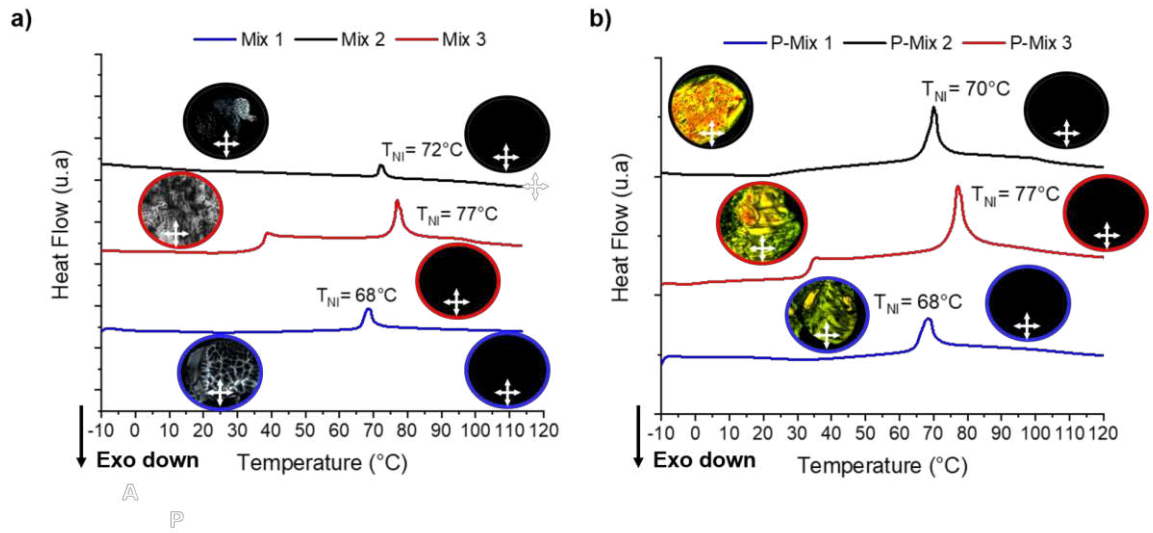

Figure S2. (a) DSC thermograms of the LC ink formulations recorded during the second

heating cycle in exo down mode, together with the corresponding POM images showing the different material phases. (b) DSC thermograms of the DR1A-containing LC formulations, accompanied by the corresponding POM images of the respective phases.

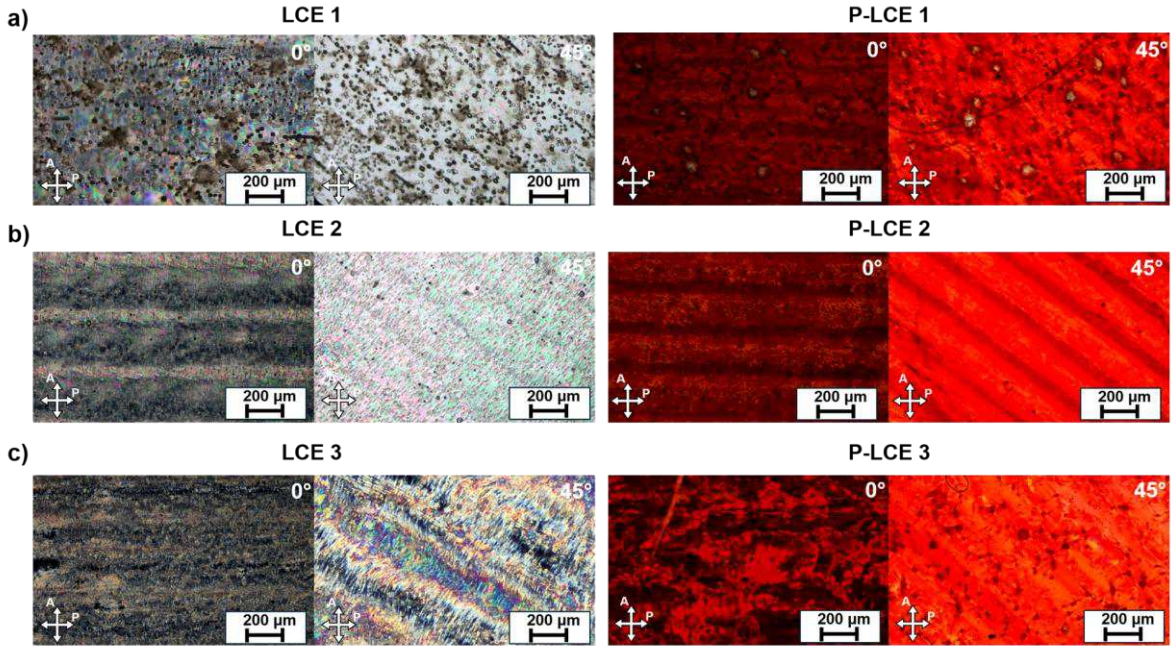

Figure S3. (a) POM images showing the molecular alignment of LCE1 on the left and P-LCE1 on the right at 0° and 45° with respect to the polarizer axis; (b-c) Corresponding POM images of LCE2 and LCE3 on the left, respectively, and P-LCE2 and P-LCE3 on the right, acquired under the same polarization conditions.

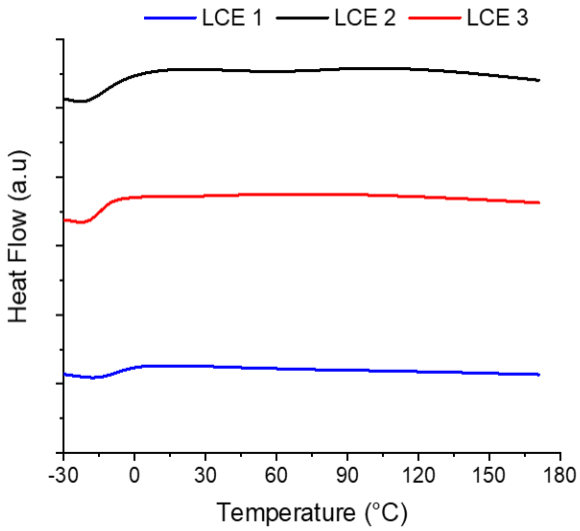

Figure S4. DSC trace of the LCEs after printing and photocuring performed at 20 °C/min.

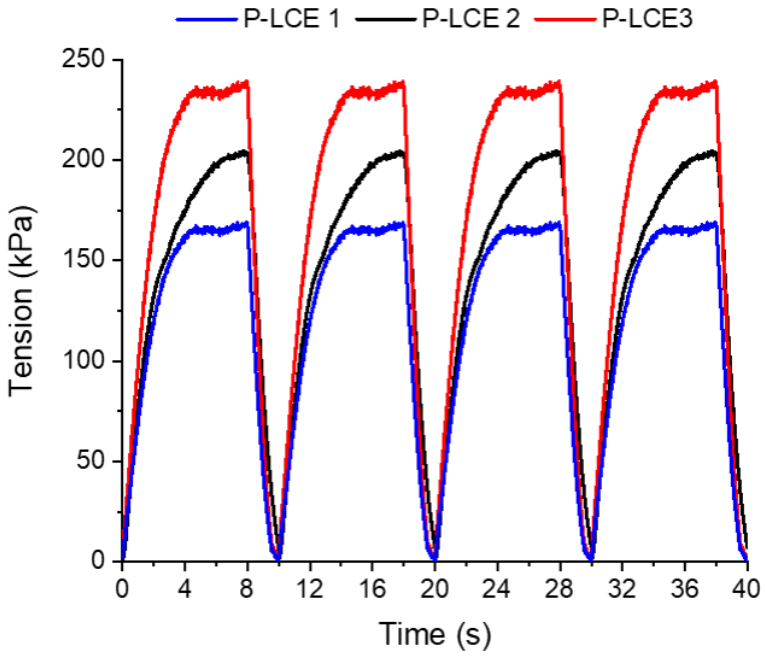

Figure S5. Cyclical activation of a 100 µm-thick LCE was performed using 8 seconds of irradiation at 15.9 mW/mm² within a 10-seconds time window.

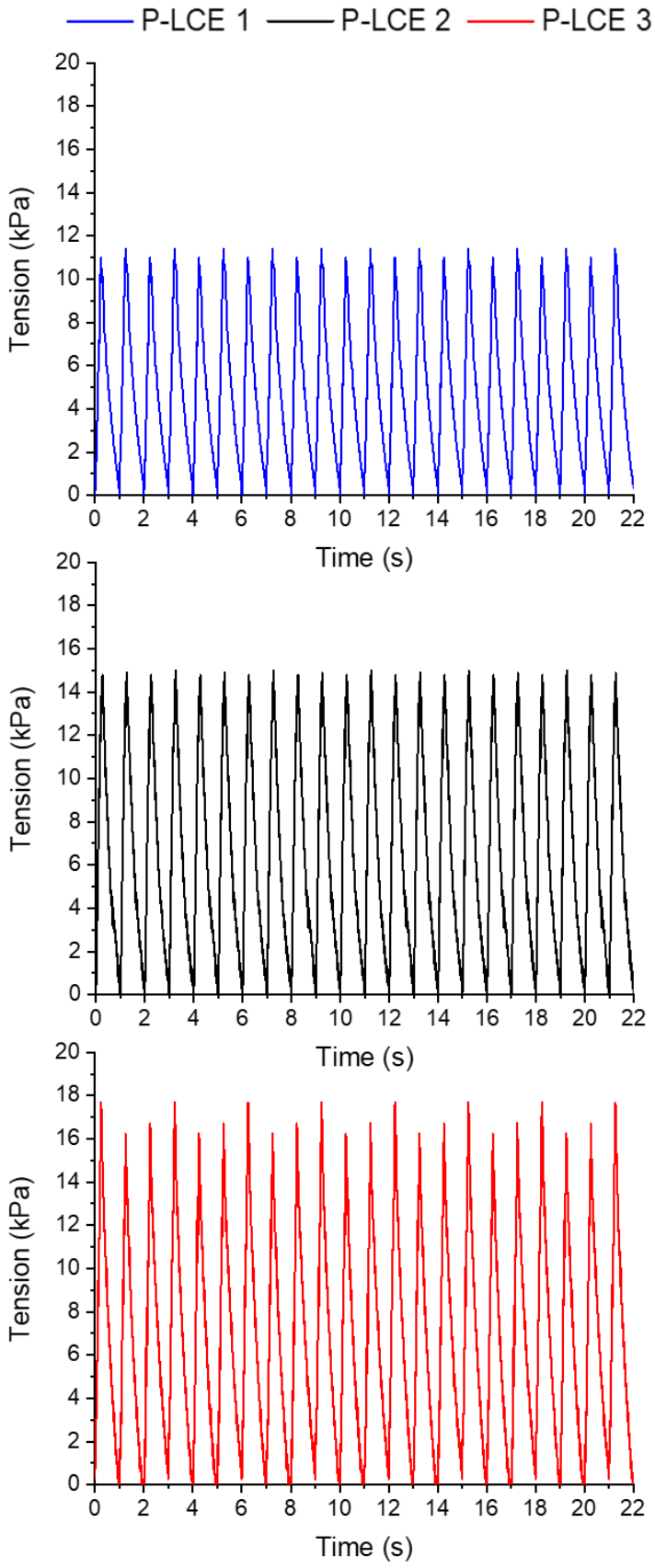

Figure S6. Cyclical activation of a 100 µm-thick LCE was performed using 250 milliseconds of irradiation at 15.9 mW/mm² within a 1-second time window.

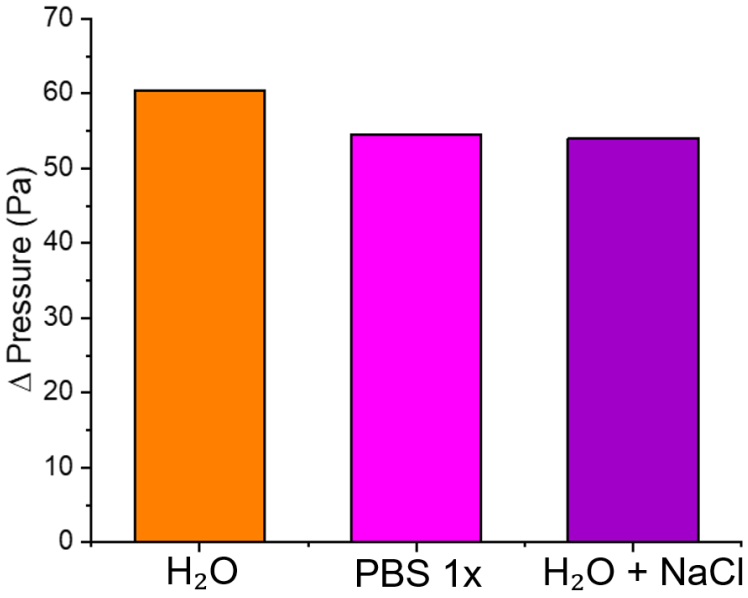

Figure S7. Bar graph showing the pressure difference developed inside the LCE soft pump as a function of the density of the transported solution during the actuation cycle.

Supplementary Files

This is a list of supplementary files associated with this preprint. Click to download.

- SupportingInformationMovieS2.mp4
- SupportingInformationMovieS1.mp4